frontiers | Frontiers in Energy Research

TYPE Original Research
PUBLISHED 19 October 2023
DOI 10.3389/fenrg.2023.1236436

OPEN ACCESS

EDITED BY
Lorenzo Ferrari,
University of Pisa, Italy

REVIEWED BY
Muhammad Wakil Shahzad,
Northumbria University, United Kingdom
Quanwen Pan,
Zhejiang University City College, China

*CORRESPONDENCE
Tao Zeng,
zengtao@ms.giec.ac.cn
Xiaohu Yang,
yangxhcsic@163.com

RECEIVED 07 June 2023
ACCEPTED 04 October 2023
PUBLISHED 19 October 2023

CITATION
Zeng T, Kobayashi N, Wu J, Li J, Deng L, Yang X and Huang H (2023), Thermodynamic analysis of mechanical booster pump-assisted sorption thermochemical heat transformer driven by low-grade heat for building applications.
Front. Energy Res. 11:1236436.
doi: 10.3389/fenrg.2023.1236436

Thermodynamic analysis of mechanical booster pump-assisted sorption thermochemical heat transformer driven by low-grade heat for building applications

Tao Zeng[1,2]*, Noriyuki Kobayashi[3], Jiatao Wu[2], Jun Li[2], Lisheng Deng[2], Xiaohu Yang[1]* and Hongyu Huang[2]

[1]Science and Technology on Thermal Energy and Power Laboratory, Wuhan 2nd Ship Design and Research Institute, Wuhan, China, [2]Guangzhou Institute of Energy Conversion, Chinese Academy of Sciences, Guangzhou, China, [3]Department of Chemical Systems Engineering, Nagoya University, Nagoya, Japan

Thermochemical heat transformers (THT) can offer the potential for efficient energy storage and upgrade based on a reversible solid-gas reaction. A mechanical booster pump (MBP)-assisted water-based sorption thermochemical heat transformer driven by low-grade solar thermal energy is proposed to handle variations in the heat demand of buildings. The MBP operates during the discharging process to adjust the magnitudes of temperature lift by compression ratio depending on the user's demands. The performances of the proposed cycle employing three different reactive salts are investigated and compared with the conventional THT cycle under various operating conditions. Results indicate that compared to the conventional THT cycle, the proposed cycle achieves a maximum temperature lift of 15–17°C, 17–19°C, and 23–26°C for $SrBr_2$, LiOH, and $CaCl_2$ in the evaporating temperature range of 20–40°C, respectively. In the same operating conditions, $SrBr_2$ demonstrates the highest energy and exergy efficiencies, while $CaCl_2$ is inferior to the others due to its greater sensible heat consumption and lower reaction heat under the studied conditions. A suggestion is put forth for enhancing the temperature lift by employing a two-stage MBP-assisted cycle that utilizes the reactive salt $SrBr_2$. Compared to the single-stage MBP-assisted cycle, the heat output temperature can be further increased by up to 3–16°C at the expense of a maximum decrease of 6.6%, 84.4%, and 9.0% in coefficient of performance (COP) based on total energy input, COP based on electricity input, and exergy efficiency, respectively, at 30°C evaporating temperature. The economic and environmental analysis indicates that the proposed system is economically and environmentally feasible and could be a promising alternative to residential water heaters.

KEYWORDS

thermochemical heat transformer, solar thermal energy, water, mechanical booster pump, thermodynamic analysis

1 Introduction

The global primary energy consumption and CO_2 emissions are expected to increase to 500% and 2200%, respectively, from 1900 to 2040 (Shahzad et al., 2017). As of 3 June 2023, 95 countries worldwide, which contribute about 78.9% of the global greenhouse gas (GHG) emissions, have communicated a net-zero target (Climate Watch, 2023). China has pledged to reach a CO_2 emissions peak before 2030 and achieve carbon neutrality by 2060 at the general debate of the 75th session of the United Nations General Assembly (Wang et al., 2022). Heating represents the primary endpoint for energy consumption. In 2021, almost half of the global final energy usage took the form of heat, with 46% being employed in buildings for space and water heating purpose (IEA, 2022). In China, the building sector represented about 22% of total primary energy consumption in 2018 and is expected to grow contentiously (Feng et al., 2021). Fossil fuel-based heaters have plummeted in recent years; however, they still falls relatively short of the carbon-neutral goal and continues to occupy the dominant position in China's existing buildings (Su and Urban, 2021). Moreover, China's building stock is predicted to climb from 47.7 billion in 2012 to 81.9 billion by 2050, and the floor space of residential buildings will reach 62.9 billion m^2 (Hong et al., 2014). Therefore, the mission to enhance energy efficiency within structures grows progressively complex and urgent for China as it strives to achieve the ambitious decarbonization objective (IEA, 2021).

Increasing the renewable energy use in buildings, such as solar thermal and geothermal energy, to meet the ever-growing heating demand will significantly influence the reduction of GHG emissions (Daneshazarian and Berardi, 2023). The solar thermal system is a well-established technology that transfers a considerable proportion of solar radiation into heat during the day, then delivered by the working medium to the consumer. However, the intermittency and fluctuations of solar energy and the spatial discrepancy between energy supply and demand constrain its widespread application and promotion (Sharma and Anil Kumar, 2017). Incorporating heat storage into buildings is recognized as a primary strategy for overcoming current barriers and enhancing the efficiency of solar energy (Vérez et al., 2023).

The heat demand varies not only by time but also by temperature. The temperature requirement may be different from user to user. Moreover, the temperature required by the same user may change depending on user needs. Therefore, one can foresee that an ecologically mindful heating system, characterized by its uncomplicated design, user-friendly operation, safety, and dependability, could deliver the desired heat output temperatures to users in alignment with their needs. Increasing attention is being paid to developing thermochemical energy storage (TCES). Compared to sensible and latent heat storage, TCES has high energy storage density, ignorable energy losses during the long storage period, and multiple operating modes (including refrigeration, combined cooling and heating production, direct heat storage and supply, and heat upgrade) based on a reversible solid-gas chemical reaction (Sharma and Anil Kumar, 2017; Li et al., 2021). Low-grade thermal energy, the most common form of waste heat and solar thermal energy, can be stored for subsequent use or upgraded to higher temperature levels that cater to building applications by thermochemical heat transformers (THT) (Li et al., 2015). Generally, according to the mode of heat upgradation, THT can be divided into two types: sorption thermochemical heat transformer (STHT) and resorption thermochemical heat transformer (RTHT) (An et al., 2022). For a single-stage STHT, the reactor packed with reactive salt is connected to a condenser or evaporator during the charging or discharging process. The sorbate (such as ammonia or water), whose operating pressure is controlled by the condenser/evaporator temperature, is exchanged between the reactor and condenser/evaporator. However, a single-stage RTHT comprises two reactors, one filled with a high decomposition temperature reactive salt, while the other has a low decomposition temperature reactive salt. At present, the development of THT is still in the research stage. Efforts to enhance the system performance and promote the commercialization of THT have mainly concentrated on the screening of suitable working pairs (Richter et al., 2018; Miche and Clausse, 2020), development of high-performance composite materials (Li et al., 2021; Nguyen et al., 2022), reactor optimization (Wyttenbach et al., 2018; Stengler et al., 2021), and advanced thermodynamic cycle.

Esaki et al. (2017) experimentally investigated the influences of the heat exchanger configurations on the heat and mass transfer performance of an STHT using $CaCl_2$ as reactive salt, and they concluded that the aluminum plate-tube heat exchanger with corrugated fins and an inserted nickel plate has the best performance among the four heat exchanger configurations. Stengler et al. (2020) experimentally surveyed the qualification of a $SrBr_2$-H_2O-based STHT for industrial waste heat storage and upgrade applications in the 150°C–300°C temperature range. The results showed that a heat source temperature of 160°C could be increased up to 260°C. Furthermore, empirical models were developed for interpreting the effective reaction rate of the hydration/dehydration process under certain conditions relevant to typical operating applications. An STHT using a working pair of $SrCl_2$-NH_3 for short-term and long-term solar heat storage and upgrade was introduced and theoretically explored by Li et al. (2015). Results indicated that a temperature lift of 16°C–50°C with energy storage density and energy upgrade efficiency higher than 1362 kJ/kg and 0.65, respectively, could be achieved at a heat of 96°C and ambient of 25°C. Although STHT can supply stable heat output temperature with high energy storage capacity, it is not a good candidate for NH_3 or H_2-based TES systems due to the high system pressure resulting from the gas and liquid phases coexisting in the same vessel.

The introduction of RTHT can enhance the system's security by replacing the condenser/evaporator with a reactor, effectively eliminating the presence of any liquid sorbate. The advantage of RTHT for energy storage and upgrade has been demonstrated by Jiang et al. (2017), who established and experimentally analyzed an RTHT using $CaCl_2$-$MnCl_2$/NH_3 as a working pair. The results indicated that the enhanced heat could still be utilized further in the industrial process, even though there might be a certain degree of deterioration in the system efficiency. Yan et al. (2020) introduced a $NiCl_2$-$SrCl_2$/NH_3 RTHT system featuring three operational modes (thermal energy upgrade mode, direct thermal energy storage and release mode, and combined cooling and heating mode) designed to regulate the supply temperature based on specific application

scenarios. The results indicated that the thermal energy upgrade mode had a thermal energy storage density of 1427.82 kJ/kg with a heat storage efficiency of 0.55 when the global conversion rate and mass ratio were 0.85 and 8, respectively. They concluded that the proposed system could provide an efficient means for energy storage and upgrading, potentially enhancing its utilization in large-scale industrial processes and renewable energy domains. In comparison to STHT, RTHT is frequently characterized by an extended cycle period due to the relatively low chemical reaction rate resulting from the low driving pressure drop. In addition, the releasing temperature may become unstable due to the discrepancy between the chemical reaction rate of the two reactive salts (Babu and Kumar, 2022).

Some advanced thermodynamic cycles are presented to overcome the shortcomings of single-stage STHT and RTHT. Li et al. (2013) proposed an innovative THT based on halide salt-ammonia working pairs by combining a pressure-reducing desorption method during the charging process and a temperature-lift adsorption method during the discharging process to reduce the driving heat source temperature and avoid the temperature fluctuation of heat released. Results revealed that the presented system is an effective way to supply various temperature levels of energy upgrade of low-grade heat energy by selecting suitable reactive salts. Fluctuations in solar radiation with time will cause unstable heat source temperatures that may not satisfy the temperature requirement of the charging or discharging process. To improve the reliability and versatility of the solar-powered energy storage system, the operating performance of a metal halide-NH_3-based thermochemical multilevel sorption thermal battery for cascading solar energy storage was evaluated (Li et al., 2016). The reactors filled with different metal halides have varying decomposition temperatures at a given operating pressure During the charging process, the heat transfer fluid (HTF) sequentially flows from the reactor with reactants of higher decomposition temperatures to the reactor with reactants of lower decomposition temperatures, leading to a significant temperature difference between the HTF and the reactants. While, during the discharging process, the HTF flows in the reverse direction compared to the charging process, moving from the reactor with reactants of lower synthesis temperatures to the reactor with reactants of higher synthesis temperatures Results indicated that the proposed technology could provide a noticeable advantage over conventional heat storage systems in terms of energy storage density and the operable temperature range of solar collection. N'Tsoukpoea et al. (2016) also theoretically analyzed the same cascaded system using salt hydrate-H_2O as working pairs in response to the requirement for high energy storage density and different temperature levels of buildings' heat demand. They pointed out that the cascade design can contribute to better energy storage density as well as higher energy and exergy efficiencies due to fewer irreversibilities. To acquire higher thermodynamic performance with a broad operating temperature range, (Mohan and Sharma, 2019) established a novel three-stage metal hydride-H_2 RTHT. They found that the proposed system could increase the COP by 66.7% compared with the conventional metal hydride-hydrogen RTHT system. Nonetheless, it is worth noting that the intricate structures and control strategies of multi-stage or cascading systems are unavoidable. Achieving a harmonious alignment of chemical reaction rates between diverse reactive salts is also challenging, potentially leading to heat output temperature instability Evaluation models were built by An et al. (2020) to provide information for the proper choice of halide-NH_3 working pairs based on single-stage sorption/resorption cycles. The results demonstrated that when the heat source temperature exhibits large fluctuations, multi-salt would be a better option for the sorption cycle from an exergetic point of view. However, it does not apply to the resorption cycle due to the uncompleted reaction of the reactive substances during the discharging process.

The merits of compression-assisted TES systems have been proved in many studies, especially in absorption heat pumps (Wu et al., 2018; Gao et al., 2021). A stable and controllable vapor pressure can be generated through a compressor, thereby ensuring a consistent heat output temperature even when the heat source temperature fluctuates. Comparatively, fewer studies focused on the hybrid compression-THT for energy storage and upgrade. Gao et al. (2019) presented a pressure boost NH_3-based THT that only used one type of reactive salt for efficient and continuous upgradation of industrial waste heat. Thermodynamic results demonstrated that the proposed cycle is superior to the vapor-compression heat pump in terms of COP and compressor discharge temperature for high-temperature applications. To further improve the heat pump performance to meet high-temperature requirements, they suggested combining pressure-boost THT using $SrCl_2$-NH_3 as the working pair with a vapor-compression heat pump. Jiang et al. (2020) conducted a comprehensive study on a hybrid $MnCl_2$-$CaCl_2$-NH_3-based RTHT, wherein they incorporated a compressor into either the charging or discharging process to achieve integrated energy storage and energy upgrading. Contrasted with a triple-stage resorption heat transformer, the potential arises for attaining heightened energy and exergy efficiencies, coupled with a diminished system volume. Besides, they came to the conclusion that the suggested hybrid system holds promise as a technique for domestic heat applications when integrated with photovoltaic-thermal systems. This is attributed to its higher global conversion rate, greater heat storage density, and enhanced energy efficiency compared to the basic RTHT without the compressor. Additionally, they carried out an evaluation and comparative analysis of the previously mentioned system alongside a fundamental RTHT that integrates internal heat recovery. This evaluation encompassed the utilization of two distinct working pairs to facilitate the seasonal storage of solar energy in an exceedingly cold region (Jiang et al., 2021). Results indicated that the proposed system exhibits potential advantages in energy efficiency and system compactness. To obtain stable heat output temperature and satisfy the user demand in various utilizations, Babu and Kumar (2022) erected a compressor driven NH_3-based RTHT in which the compressor was installed between the two reactors to compress the desorbed NH_3 vapor from the HTS reactor to the LTS reactor during the discharging process. The system performances were theoretically evaluated and contrasted by employing different combinations of halide salts under different cooling temperatures and compression ratios for heat storage, combined cooling, and heat upgradation. Finally, suitable halide salts for low and medium-temperature energy storage have been recommended.

The literature review above indicates that most of the studies concentrated on theoretical or experimental investigations of THT

systems based on NH_3. These studies aimed to achieve a broader working temperature range and higher, consistent heat release temperatures even when faced with fluctuating heat source temperatures. Their feasibility and potential have been demonstrated for low-grade energy storage and upgrade, particularly in industrial applications. However, the safety issue, the large volume, and the complicated control strategies (in the case of a multi-stage or cascading system) make NH_3-based THT unsuitable for building applications. Besides ammonia, water is another commonly studied sorbate for TES systems due to its desirable properties, such as being environmentally friendly, good thermal stability, non-toxicity, and non-flammability. Despite the advantages mentioned above, some challenges still need to be surmounted when using water as sorbate (Bamigbetan et al., 2017). For example, the low vapor pressure (especially when the heat source temperature is below 100°C) will cause poor mass transfer performance, air leakage, and high compressor discharge temperature. Mechanical booster pump, also popularly known as roots compressor, is a rotary positive displacement pump based on mechanical principles and can be a suitable choice for the proposed system. In contrast to rotary vane and dry pumps, MBPs are not oil sealed. Two symmetrically shaped lobes are sealed by a tightly controlled gap and counter-rotate inside the pump casing without contact (Hong et al., 2018). Thus, the working vapor will not be contaminated by lubricating oil. Hong et al. (2018) experimentally and numerically investigated the thermal performance of a mechanical vapor compression system driven by MBP from the point of industrial operation. In prior work by the authors, the experimental feasibility of an MBP-assisted adsorption chiller cycle has been investigated and demonstrated (Zeng et al., 2017). To the best of our knowledge, there have been limited efforts in developing THT systems assisted by compressors and utilizing water as the working fluid.

Our previous study has proposed a mechanical booster pump (MBP)-assisted water-based STHT in response to variations in heat input temperature during the charging and discharging processes when using low-grade heat as a driving force (Zeng et al., 2022). As an extension of the evaluations in our previous work, this study focuses on the heat output performance of the MBP-assisted water-based STHT when the heat input temperature is stable at a relatively low level. This situation commonly occurs when the solar heat from the solar collector is partially collected in the storage tank (the remaining part is applied to drive the charging process) during the day. Yet, throughout the night, the water temperature within the storage tank remains relatively stable and situated at a lower point. This leads to the conventional THT's temperature output having limited flexibility in responding to variations in heat demands. This is the issue we intend to address. In this study, $SrBr_2$, LiOH, and $CaCl_2$ have been chosen as the reactive material due to their high energy storage density, favorable reaction temperature, and excellent chemical stability (Wei et al., 2020; Ding et al., 2021; Li et al., 2021).

This paper is structured as follows. Firstly, in Section 2, we illustrate the working principle of the single-stage MBP-assisted STHT, followed by an explanation of the methodology and the assessment of performance indicators. Results and discussion are indicated in Section 3. Based on the above results, a two-stage MBP-assisted STHT is also proposed and evaluated in Section 3 to further upgrade the heat output temperature. Moreover, the economic feasibility and CO_2 emissions reduction potential of MBP-assisted STHT are studied and compared with the residential water heaters. Section 4 is devoted to the conclusion. The heat output temperature, energy, and exergy efficiencies are comprehensively investigated and compared under the different heat source temperatures, reaction advancements, and compression ratios. In addition, the advantages and feasibility of the proposed system are further elucidated by comparison with conventional STHT.

2 Methodology

2.1 MBP-assisted STHT cycle

The simplified representation of the proposed system is schematically illustrated in Figure 1, and the corresponding P-T diagram using $CaCl_2$·(1-2)H_2O-H_2O as working pair is shown in Figure 2. The equilibrium lines of the water liquid-vapor and the solid-gas thermochemical reaction are monovariant and follow the Clausius-Clapeyron relation.

$$\ln\left(\frac{P}{P_0}\right) = -\frac{\Delta H_r}{RT} + \frac{\Delta S_r}{R} \tag{1}$$

where P and T represent, respectively, the equilibrium pressure and temperature of the liquid-gas phase transition or solid-gas reaction; P_0 is the reference pressure, kPa; R is the ideal gas molar constant, J/(mol·K); ΔH_r and ΔS_r represent the standard enthalpy of reaction [J/mol] and the standard entropy of reaction [J/(mol·K)] per mole of water vapor, respectively.

The MBP-assisted STHT cycle shares the same charging process as the conventional one and thus operates under identical conditions. Throughout the on-sun period, a fraction of the solar heat gathered by the solar collector is employed to supply the necessary heat for the dehydration reaction. Meanwhile, the other portion is stored in the storage tank or directed to the end-user. As shown in Figure 1A, during the charging process, the reactor packed with hydrated salt is heated by the circulating HTF with a temperature of T_1 being supplied from the solar thermal collector. The hydrated salt undergoes dehydration and converts into anhydrous or less hydrous state, resulting in the storage of solar heat energy in the form of chemical bonds. The resultant water vapor flows into the condenser at the pressure of P_1 and then condenses back into liquid at T_2, as indicated in Figure 2. The condensation heat is discharged into the atmosphere.

During the discharging process, referring to Figure 1B, the condenser/evaporator at ambient temperature T_2 is firstly heated up to the evaporating state ③ by the low-temperature heat at T_3 from the storage tank, resulting in a heat consumption of Q_{s1}. Subsequently, the water within the evaporator evaporates according to the liquid-gas equilibrium at temperature T_3 and the corresponding pressure, P_m. In the case of a conventional cycle, the water vapor moves directly into the reactor at P_m, where it is absorbed by the anhydrous or less hydrous salt, resulting in the generation of heating effect Q_4. Due to the monovariant characteristic of hydration reaction, the releasing heat temperature can only be obtained up to T_4, which may not meet the requested heat demands. For the MBP-assisted STHT cycle, however, an MBP is employed and installed between the evaporator

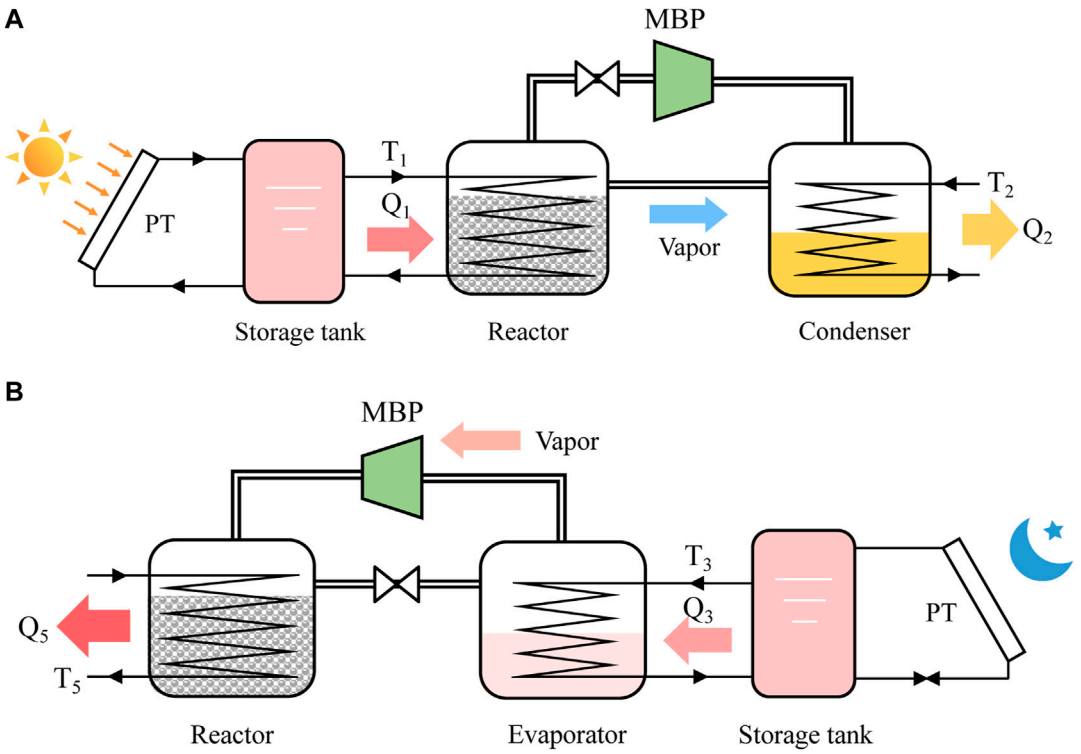

FIGURE 1
Schematic of MBP-assisted H_2O-based STHT system **(A)** charging process during the on-sun period, **(B)** discharging process during off-sun period.

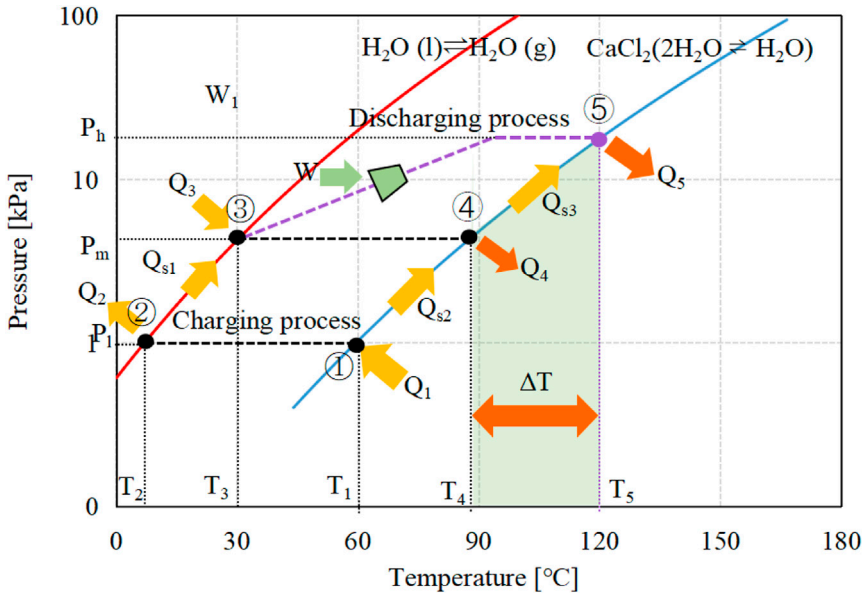

FIGURE 2
P-T diagram of MBP-assisted H_2O-based STHT system using $CaCl_2$·(2-1)H_2O as an instance.

and the reactor, as can be observed from Figure 1B. The water vapor generated is pressurized by the MBP from P_m to a higher pressure level of P_h and subsequently transferred into the reactor to react with the reactive salt. The hydration heat Q_5 is released at T_5, which can be easily adjusted in response to the heating demand requirement of the end-user by controlling the compression ratio of MBP at the cost

TABLE 1 Thermodynamic parameters for reactive materials (Zeng et al., 2022).

Reactive materials	Cp [J/mol/K]	ΔH [kJ/mol-H_2O]	ΔS [J/mol/K]
H_2O	34.5 (vapor)	43.3	116
	4.2 (liquid)		
$LiOH/LiOH{\cdot}H_2O$	49.7 (LiOH)	64.3	161
	79.6 ($LiOH{\cdot}H_2O$)		
$SrBr_2{\cdot}H_2O/SrBr_2{\cdot}6H_2O$	121 ($SrBr_2{\cdot}H_2O$)	67.4	175
	344.8 ($SrBr_2{\cdot}6H_2O$)		
$CaCl_2{\cdot}H_2O/CaCl_2{\cdot}2H_2O$	108 ($CaCl_2{\cdot}H_2O$)	51.2	145
	172.4 ($CaCl_2{\cdot}2H_2O$)		

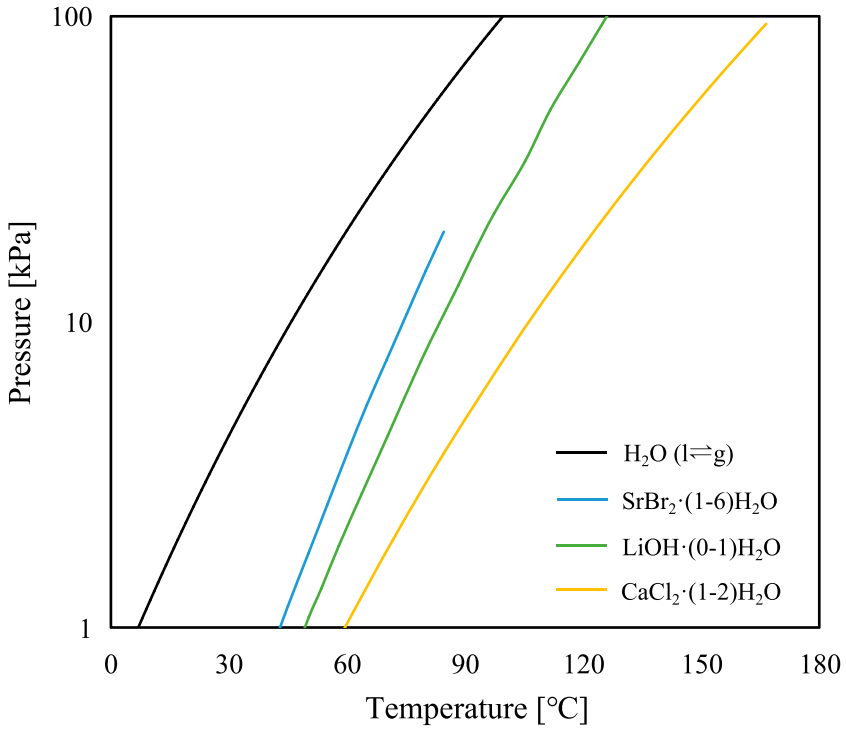

FIGURE 3
Thermodynamic equilibrium of pure water and the three selected reactive salts ($SrBr_2{\cdot}(1\text{-}6)H_2O$, $LiOH{\cdot}(0\text{-}1)H_2O$, and $CaCl_2{\cdot}(1\text{-}2)H_2O$).

of off-peak electricity consumption. Compared to conventional STHT cycles, i.e.,①-②-③-④-①, higher heat output temperature can be obtained by the proposed cycle ①-②-③-⑤-① with a temperature lift of ΔT at the same heat source temperature (as highlighted in the green shade in Figure 2) and thus a more flexible and reliable system. This is precisely the focus of this study.

It is noteworthy to mention that part of the hydration heat produced during the discharging process is consumed to warm up the reactor from ambient temperature T_2 to the desired heat output temperature, T_4 for the conventional cycle with a heat consumption of Q_{s2} and T_5 for the proposed one with a heat consumption of $Q_{s2}+Q_{s3}$. Once the discharging process is complete, the reactor and evaporator naturally cool down to the ambient temperature in readiness for the subsequent charging process.

2.2 Mathematical model

The reversible thermochemical reactions of the three selected salts with water vapor can be expressed as follows:

$$SrBr_2 \cdot H_2O\,(s) + 5H_2O\,(g) \Leftrightarrow SrBr_2 \cdot 6H_2O\,(s) + 5\Delta H_r \quad (2)$$

$$LiOH\,(s) + H_2O\,(g) \Leftrightarrow LiOH \cdot H_2O\,(s) + \Delta H_r \quad (3)$$

$$CaCl_2 \cdot H_2O\,(s) + H_2O\,(g) \Leftrightarrow CaCl_2 \cdot 2H_2O\,(s) + \Delta H_r \quad (4)$$

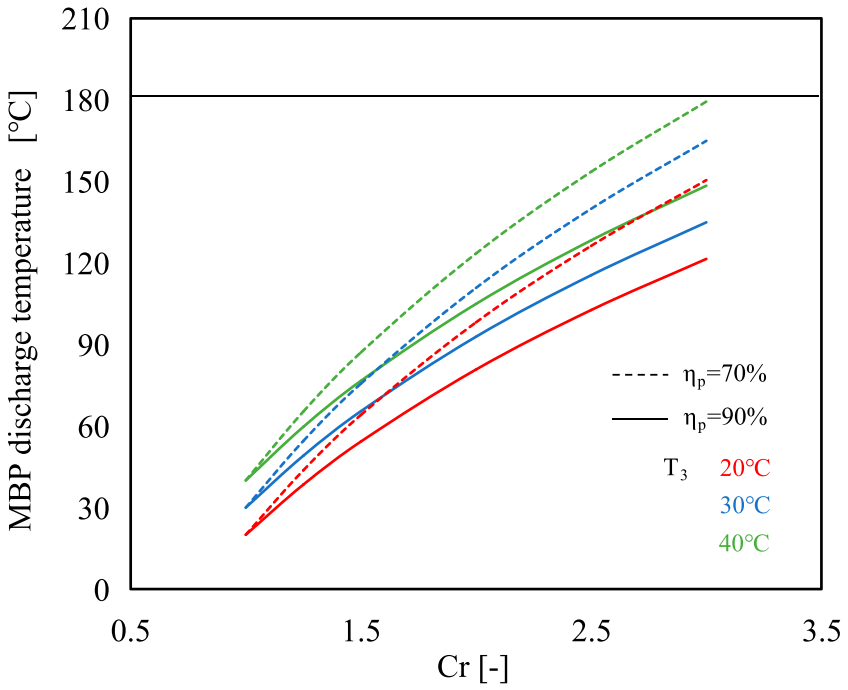

FIGURE 4
Variations of MBP discharge temperature with compression ratio at different evaporating temperatures and MBP isentropic efficiencies.

The equilibrium P-T lines of the three distinct working pairs are calculated using their respective thermodynamic properties (Table 1) and are depicted in Figure 3.

In this study, the ambient temperature is chosen as 2°C according to the winter climatic conditions of Guangzhou in southeast China, with an average minimum temperature of 10°C. While the corresponding minimum charging temperature T_1 required for $SrBr_2{\cdot}6H_2O$, $LiOH{\cdot}H_2O$, and $CaCl_2{\cdot}2H_2O$ is 43°C, 50°C, and 60°C, respectively, as determined from Eq. 1. It is believed that a flat-plate collector, the most widely utilized solar hot water device for low-temperature applications, can meet these temperature demands of the charging process. This collector has an applicable temperature range of 70°C–90°C on sunny days (Di Fraia et al., 2022). Considering some severe conditions such as the thermal loss from the storage tank or insufficient heat storage in the storage tank, the nighttime low-temperature heat source at night is set to be 20°C–40°C.

In the present study, we have modified the theoretical model as established in the previous study (Zeng et al., 2022) and hypothesized the following.

(1) The system operates under steady-state conditions.
(2) The mass of anhydrous or less hydrous reactive salt is assumed to be 2 kg.
(3) The isentropic efficiency of MBP is taken as 70%.
(4) The thermal losses of the whole system are ignored.
(5) The heat input temperature is high enough for the charging process during the daytime that the reactive salts can dehydrate completely.
(6) The temperature distribution inside the components is uniform, and the temperature difference between the outlet and inlet of HTF is 0°C.
(7) The thermal mass of the component is factored in on a one-to-one basis.
(8) Pressure drop through the pipelines and reactive salts is negligible.
(9) Thermodynamic properties of reactive salt are constant during the cycle.
(10) The hysteresis between the hydration and dehydration equilibrium curves is negligible.
(11) The evaluation of system efficiency does not include the powers of the HTF pumps.

The equation below provides the required heat input for the reactor during the charging process:

$$Q_1 = \Delta H_r \Delta N_{H_2O} \eta_r + \frac{\Delta N_{H_2O}}{\nu_{H_2O}} (T_1 - T_2)\left[c_{p,M\cdot yH_2O}(1-\eta_r) + c_{p,M\cdot(x+y)H_2O}\eta_r\right] + c_{p,r} m_r (T_1 - T_2) \quad (5)$$

where the first term on the right indicates the dehydration reaction heat, kJ; the second and the third terms are respectively the sensible heat of the reactive salt and the reactor metal during the charging process, kJ; η_r is the reaction advancement indicating the degree of completeness of the reaction, and can be obtained by dividing the actual molar amount of released or adsorbed water vapor at any moment during the process with the theoretical molar amount of water vapor; ΔN_{H2O} is the theoretical molar amount of water vapor released from the hydrated salt $M{\cdot}(x+y)H_2O$ during the charging process or adsorbed by the anhydrous or less hydrous salt $M{\cdot}yH_2O$ within the discharging period, mol; $c_{p,M\cdot xH2O}$,

$c_{p,M\cdot(x+y)H2O}$ and $c_{p,r}$ are the specific heat of anhydrous or less hydrous salt, hydrated salt and reactor metal (stainless steel 316 is considered in this study), respectively, kJ/(mol·K); v_{H2O} is the stoichiometric coefficient of H_2O in the thermochemical reaction; m_r is the mass of the reactor metal, kg; subscripts "1″and "2″stand for the corresponding points ① and ② shown in Figure 2, respectively.

The sensible heat needed to raise the liquid water from the ambient temperature to the evaporating temperature in the preheating process ②→③ is expressed as:

$$Q_{s1} = c_{p,l}\Delta N_{H_2O}(T_3 - T_2) \tag{6}$$

where $c_{p,l}$ denotes the specific heat of liquid water, kJ/(mol·K); The subscripts "3″corresponds to the evaporating point ③ shown in Figure 2.

The equations below allow us to calculate the beneficial heat output from the reactor when in the discharging process:

$$Q_3 = \Delta H_{vap}\Delta N_{H_2O}\eta_r \tag{7}$$

where ΔH_{vap} is the vaporization enthalpy of water, kJ/mol.

The useful heat output from the reactor during the discharging process can then be obtained by the following equations:

For the MBP-assisted STHT cycle,

$$\begin{aligned} Q_5 = {} & \Delta H_r\Delta N_{H_2O}\eta_r \\ & - \frac{\Delta N_{H_2O}}{\nu_{H_2O}}(T_5 - T_2)\left[c_{p,M\cdot yH_2O}\eta_r + c_{p,M\cdot(x+y)_{H_2O}}(1-\eta_r)\right] \\ & - c_{p,v}\eta_r\Delta N_{H_2O}(T_5 - T_d) - c_{p,r}m_r(T_5 - T_2) \end{aligned} \tag{8}$$

where the first term on the right describes the hydration reaction heat, kJ; the second term represents the sensible heat needed to elevate the temperature of the reactive salt from the surrounding temperature to the output temperature T_5, kJ; the third term is the heat required by the outlet vapor from MBP when it is heated up from the MBP discharge temperature T_d (calculated by Eq. 11) to the output temperature T_5, kJ; the fourth term is sensible heat consumption of the reactor mass during the discharging process, kJ; $c_{p,v}$ is the specific heat of water vapor at MBP discharge, kJ/(kg·K). Of particular interest is that when T_d surpasses T_5, the third term will positively influence the increase of Q_5. For the conventional STHT cycle, the heat output temperature should be T_4 rather than T_5, and the MBP discharge temperature T_d needs to be replaced by the evaporating temperature T_3, as shown in Figure 2.

The actual power of the MBP in kJ can be obtained by the following equation:

$$W_p = \frac{\Delta N_{H_2O}\eta_r RT_3}{\eta_p}\frac{k}{k-1}\left[(Cr)^{\frac{k-1}{k}} - 1\right] \tag{9}$$

where η_p is the isentropic efficiency of MBP; k is the adiabatic index, 1.33 for water; Cr is the compression ratio of MBP and defined as the ratio of MBP's discharge pressure (P_h) to suction pressure (P_m) as follows:

$$Cr = \frac{P_h}{P_m} \tag{10}$$

The discharge temperature of MBP is obtained by

$$T_d = T_3 + \frac{T_3 C_r^{\frac{k-1}{k}} - T_3}{\eta_p} \tag{11}$$

The coefficient of performance (COP) based on the total energy input (COP_t) and the electricity input (COP_e) are employed to evaluate the system performance in the view of the first law of thermodynamics and are respectively illustrated by Eqs 12, 13:

$$COP_t = \frac{Q_5}{Q_1 + Q_3 + Q_{s1} + Q_{s2} + Q_{s3} + W_p} \tag{12}$$

where Q_{s1}+Q_{s2}+Q_{s3} represents the sum of the second to fourth terms in Eq. 8.

$$COP_e = \frac{Q_5}{W_p} \tag{13}$$

Based on the second law of thermodynamics, exergy efficiency is defined as:

$$\eta_{ex} = \frac{\text{Output exergy}}{\text{Input exergy}} = \frac{Q_5\left(1 - T_2/T_5\right)}{\begin{aligned} & Q_1\left(1 - T_2/T_1\right) + (Q_{s1} + Q_3)\left(1 - T_2/T_3\right) \\ & + (Q_{s2} + Q_{s3})\left(1 - T_2/T_5\right) + W_{p,t} \end{aligned}} \tag{14}$$

3 Results and discussion

3.1 Effect of compression ratio on MBP discharge temperature and heat output temperature

The efficient operation of the proposed system is influenced by a crucial parameter: the discharge temperature of the MBP. In this study, the maximum discharge vapor temperature of MBP is set as 180°C to ensure the protection of the MBP unit. Figure 4 shows the MBP discharge temperature under different evaporating temperatures when the Cr varies from 1.0 to 3.0. It is indicated that the discharge temperature of MBP increases with increasing Cr and evaporating temperature while decreasing with the increase of MBP isentropic efficiency, which can be described by Eq. 11. It can be verified that the discharge temperatures of the MBP can be upheld below the maximum permissible limit across all analyzed conditions. In the subsequent investigation, the isentropic efficiency of the MBP is assumed to be 70%, while the Cr varies within the range of 1.0–3.0.

Figures 5A–C presents the heat output temperatures of the proposed system as a function of Cr at different evaporating temperatures of 20°C, 30°C, and 40°C. It can be found that the heat output temperature increases with the increase of Cr, which leads to a higher vapor pressure in the reactor. Taking $SrBr_2$ as reactive salt as an example, the heat output temperature rises from 62°C to 78°C when the Cr increases from 1.0 (i.e., the conventional STHT cycle) to 3.0 at the evaporating temperature of 30°C, indicating that the heat output temperature can be regulated in response to the heating demand by altering Cr. In addition, the higher the evaporating temperature, the greater the heat output

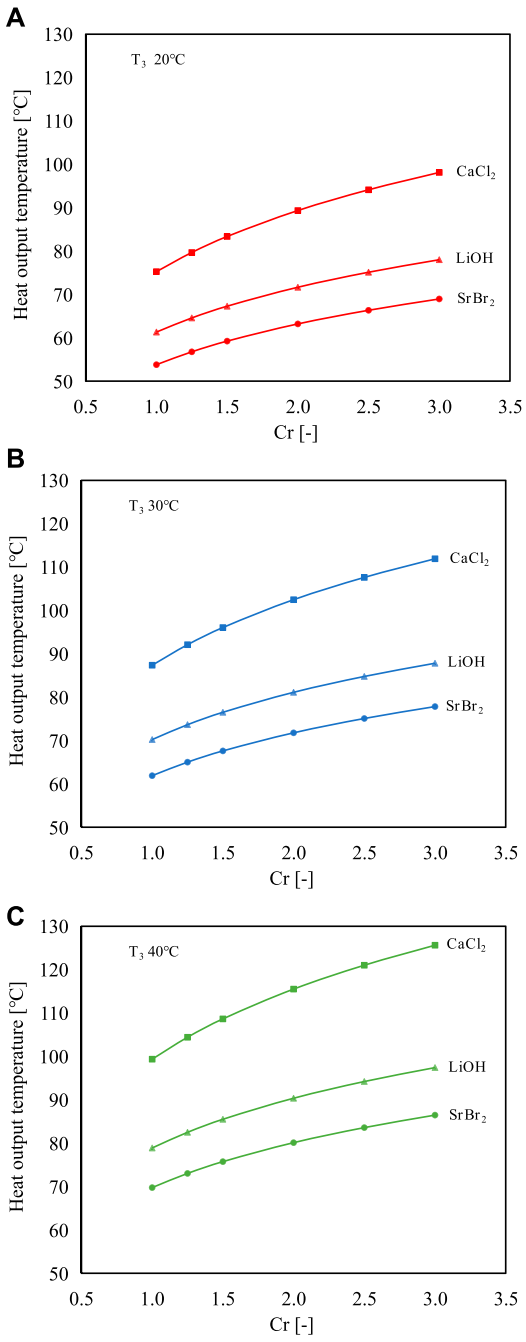

FIGURE 5
Effects of compression ratio on the heat output temperatures of the proposed cycle using three different working pairs at the evaporating temperature of **(A)** 20°C, **(B)** 30°C, and **(C)** 40°C.

temperature under the same Cr. For instance, as the evaporating temperature increases from 30°C to 40°C, the heat output temperature will increase from 78°C to 86°C at Cr of 3 when using $SrBr_2$ as reactive salt. $CaCl_2$ has the highest heat output temperature among the three reactive salts, followed by LiOH and $SrBr_2$ at the same operating condition.

The temperature lifts relative to the evaporating temperature (T_5-T_3) are presented in Figure 6. $CaCl_2$ exhibits the highest ability to upgrade the low-grade heat with a temperature lift range of 55°C–86°C when the evaporating temperature varies from 20°C to 40°C. In comparison, $SrBr_2$ and LiOH have lower temperature upgrade capacity with a temperature lift range of 30°C–49°C and 39°C–58°C, respectively. Consequently, $CaCl_2$ is more applicable for high-temperature applications. Furthermore, it can be observed that the temperature lifts of $SrBr_2$ and LiOH at high evaporating temperatures are less than those at low evaporating temperature conditions. However, $CaCl_2$ exhibits the opposite trend. This is attributed to the fact that the slope of the solid-gas equilibrium curve of $CaCl_2$ is smaller than that of the liquid-gas equilibrium curve of water resulting in the distance between these two curves becoming more pronounced with increasing evaporating temperature (i.e., the abscissa). In contrast, the opposite is true for the cases of $SrBr_2$ and LiOH, as seen in Figure 3.

3.2 Effect of reaction advancement on the system efficiencies of single-stage MBP-assisted cycle

Figures 7A–C exhibits the energy and exergy efficiencies of the proposed system based on the reaction advancement when the Cr is set as 2.0. It is clear that as the reaction progresses further, the system can achieve higher efficiencies. For example, as the reaction advancement changes from 0.1 to 1, the COP_e, COP_t, and η_{ex} increase from 4.89, 0.06, and 0.08 to 24.89, 0.54, and 0.86, respectively, when using $SrBr_2$ as reactive salt at the evaporating temperature of 20°C. However, suffering from heat and mass transfer performance limitations, the reaction advancement could hardly reach 100% under practical operating conditions. Typically, in a thermochemical reaction, the extent of reaction advancement is frequently controlled within the range of 0.7–0.9. In addition, the proposed system can achieve better energy and exergy performances at lower evaporating temperatures regardless of the reactive salt employed. This is due to the increase in evaporating temperature leading to the rise of sensible heat consumption (Q_{s1}, Q_{s2}, and Q_{s3}) and electricity consumption of MBP, while the decrease in heat output, as indicated in Eqs 12–14.

It is worth acknowledging that a threshold exists in the progression of the reaction, beyond which the energy and exergy efficiencies hold values greater than zero. In other words, this is the threshold at which the proposed system can operate normally. This is because the reaction heat is less than the sensible heat required to heat the liquid water, reactive salt, and reactor metal to the heat output temperature when the reaction advancement is small. Compared to the other two reactive salts, Contrasted with the other two reactive salts, $SrBr_2$ showcases a lower threshold value, guaranteeing the proper operation of the system. For the evaporating temperature of 30°C and Cr of 2.0, the threshold values are about 0.1, 0.11, and 0.41 for $SrBr_2$, LiOH, and $CaCl_2$, respectively. There are two reasons for why $CaCl_2$ requires a much higher level of reaction advancement to ensure proper system performance. An explanation for this is that a system that utilizes $CaCl_2$ consumes more sensible heat in contrast to employing $SrBr_2$ or LiOH as the reactive salt. This can be attributed to $CaCl_2$ generating a higher heat output temperature at the same evaporation temperature, leading to increased temperature differences of (T_5-T_2) and (T_5-T_d) as indicated in Eq. 8. Another

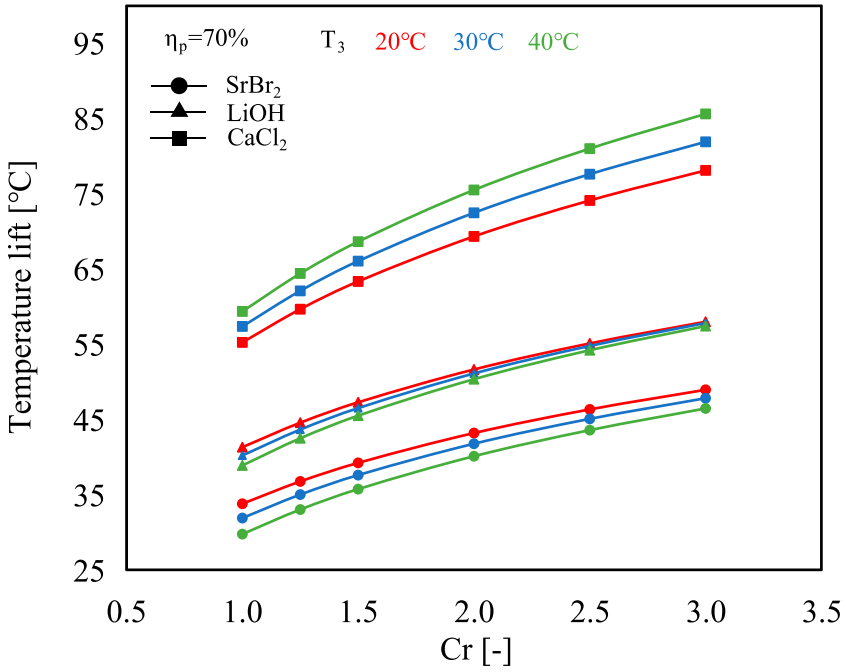

FIGURE 6
Comparison of the temperature lift of the three different working pairs under various operating conditions.

reason is that the reaction heat of $CaCl_2$ is much smaller than that of the other two salts under the set condition, i.e., they share identical mass, which leads to a lower molar amount of water (37.7 mol, 83.5 mol, and 15.5 mol for $SrBr_2$, LiOH, and $CaCl_2$ respectively when their masses are assumed to be 2 kg). The combined effect of these two factors brings about a higher threshold in $CaCl_2$. For these reasons, the performance differences between various evaporating temperatures at the same level of reaction advancement are more significant in the case of $CaCl_2$. For instance, at the reaction advancement of 0.8, when the evaporating temperature increases from 20°C to 40°C, the exergy efficiencies decrease by about 3.4%, 4.5%, and 23.9% for $SrBr_2$, LiOH, and $CaCl_2$, respectively.

3.3 Effect of compression ratio on the system efficiencies of single-stage MBP-assisted cycle

In the following study, we hypothesized that the reaction advancement is 0.8. Figure 8 presents the effects of Cr on system efficiencies under different evaporating temperatures for the three reactive salts. As depicted in Figure 8A, as Cr increases, COP_e decreases due to the higher Cr, which results in greater electricity consumption of MBP. Under the same operating condition, the COP_e of $SrBr_2$ is superior to the other two reactive salts. Although the system with LiOH as reactive salt has the highest reaction heat due to its largest mole number of hydrated water, the sensible heat required by the liquid water to reach the evaporating state and the amount of electricity consumed by the MBP also grow proportionately with the mole number of hydrated water. When it comes to $CaCl_2$, the interplay between its low reaction heat and relatively higher sensible heat consumption results in a decreased COP_e, even though it possesses the lowest electricity consumption for MBP among the three reactive salts COP_es change from 78.8 to 13.7, 73.0–12.6, and 40.1–5.2 for $SrBr_2$, LiOH, and $CaCl_2$, respectively, when the Cr increases from 1.25 to 3.0. In general, the attained COPe is higher or on par with that of a traditional vapor compression heat pump within the examined circumstances.

It can be seen that COP_ts slightly increase with the increasing Cr for $SrBr_2$ and LiOH, while $CaCl_2$ exhibits a contrary tendency, as shown in Figure 8B. The reasons can be divided into two aspects. On the one hand, with the increment of Cr, the discharge temperature of MBP increases (as presented in Figure 4), resulting in the reduction of sensible heat consumed by discharge vapor (the third term in Eq. 8). For example, the MBP discharge temperature is 165°C under the evaporating temperature of 30°C and Cr of 3.0; the corresponding theoretical heat output temperatures are 78°C and 112°C for $SrBr_2$ and $CaCl_2$, respectively. Consequently, the positive effect of the high-temperature MBP discharge vapor on the heat output would be more significant in a system employing $SrBr_2$ than that of $CaCl_2$. This results from the increased temperature difference of (T_5-T_d), as demonstrated in Eq. 8. On the other hand, as Cr increases, the heightened output temperature leads to an increase in the temperature difference between (T_5-T_2). As a result, the reactive salt and reactor mass would necessitate a larger quantity of sensible heat, as indicated by the second and fourth terms in Eq. 8. These two aspects competitively affect the variation of COP_t with Cr. Regarding $SrBr_2$ and LiOH, the positive impact arising from the high-temperature vapor discharge of MBP assumes a more crucial role as Cr increases, contributing significantly to the heat output. However, in the case of $CaCl_2$, the larger temperature difference of (T_5-T_2) brings about a more pronounced negative impact due to

10.3389/fenrg.2023.1236436

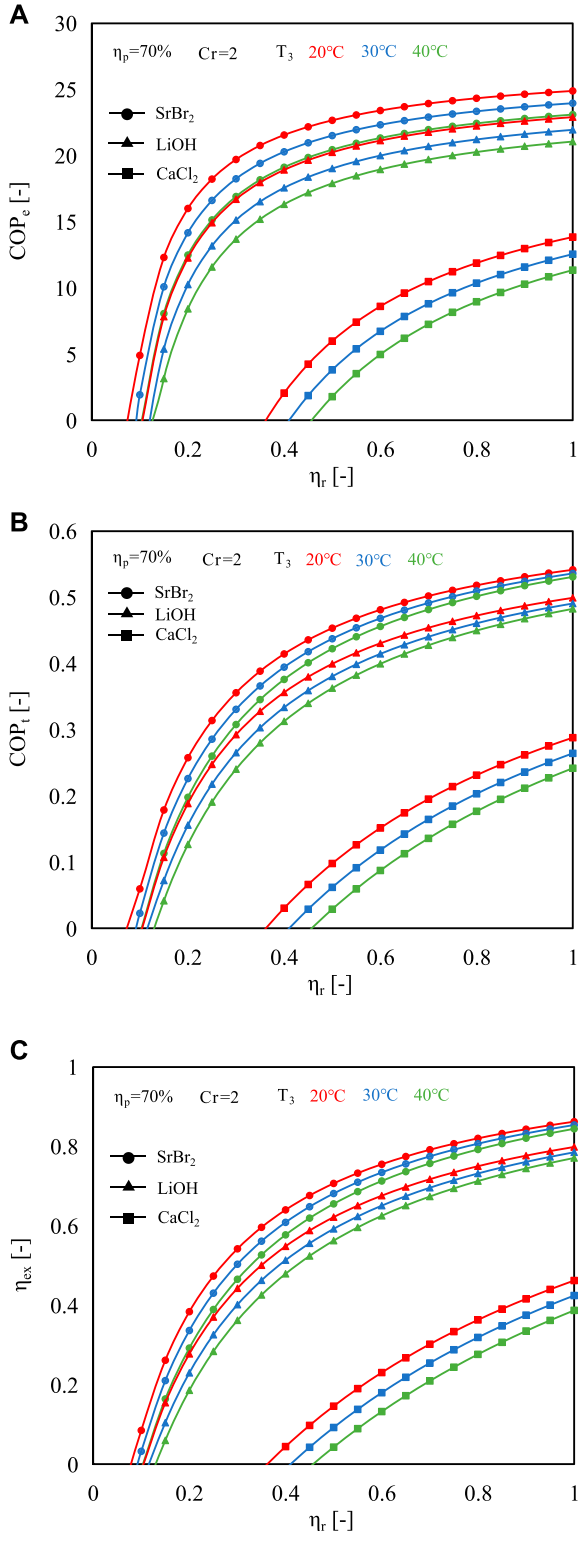

FIGURE 7
Effect of reaction advancement on **(A)** COP_e, **(B)** COP_t, and **(C)** η_{ex} at different evaporating temperatures (Cr = 2).

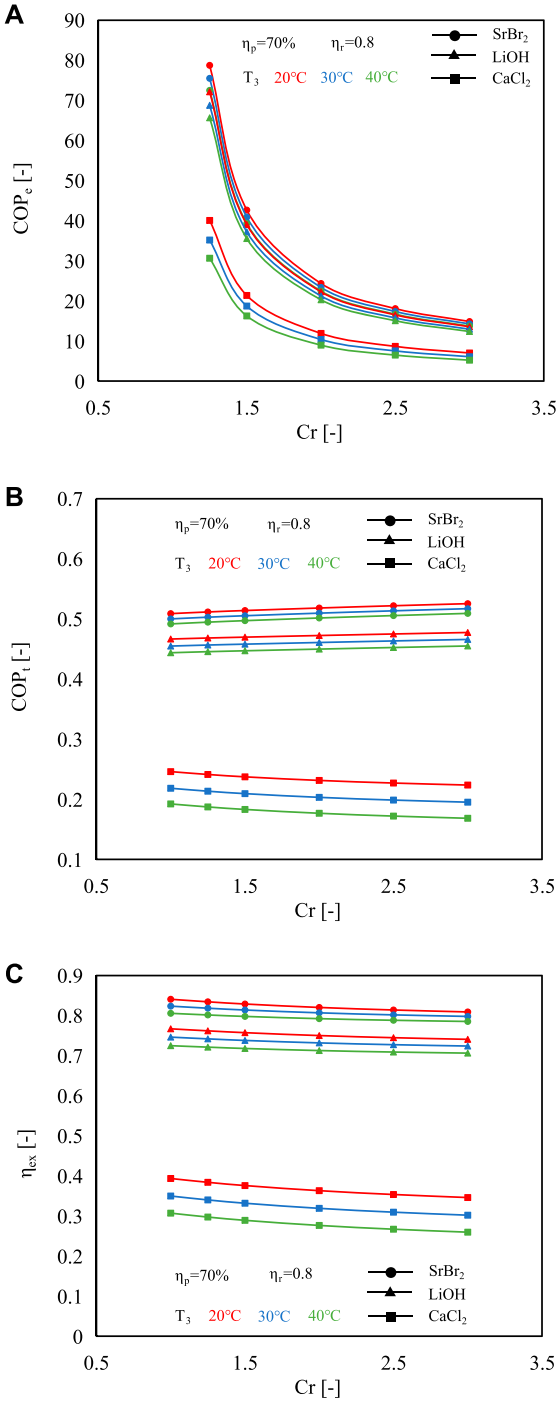

FIGURE 8
Effect of compression ratio on **(A)** COP_e, **(B)**COP_t, and **(C)** η_{ex} at different evaporating temperatures (η_r = 2).

the increasing sensible heat demand of the reactive salt and reactor mass as Cr changes. This leads to a distinct behavior compared to the other two reactive salts.

Figure 8C indicates that the η_{ex} decreases slightly with rising Cr, which is different from that of COP_t when using $SrBr_2$ and LiOH as reactive salts when considering the quality of energy. Compared to the influence of the evaporation temperature, as depicted in Figure 7C, Cr demonstrates a lesser impact on system performance, particularly in the case of $CaCl_2$, which is more affected by changes in the evaporation temperature. For instance,

10.3389/fenrg.2023.1236436

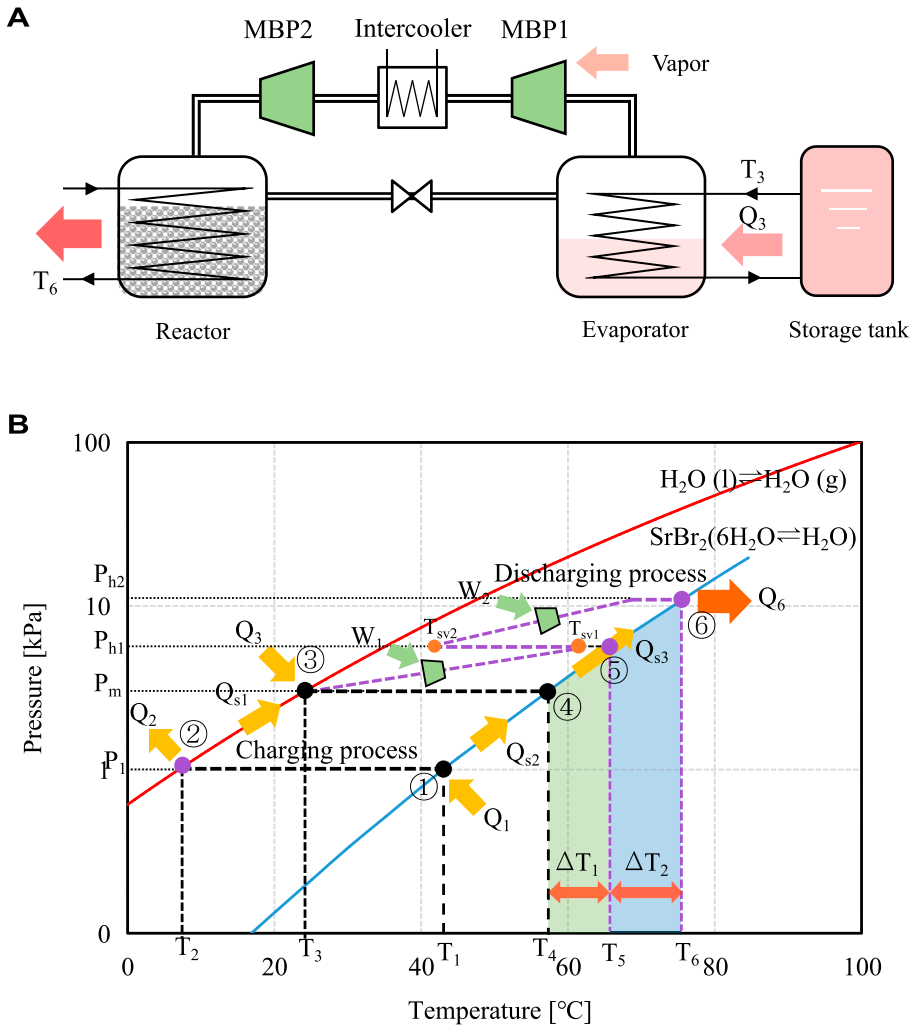

FIGURE 9
Schematic **(A)** and P-T diagrams **(B)** of two-stage MBP-assisted STHT cycle with intercooler using $SrBr_2$·(1-6)H_2O as reactive salt.

the exergy efficiencies reduces by about 3.1%, 2.6%, and 13.7% for $SrBr_2$, LiOH, and $CaCl_2$, respectively, as Cr varies from 1.0 to 3.0 at the evaporating temperature of 30°C. Therefore, evaporating temperature appears to be the most dominant factor that affects COP_t and η_{ex} when using $CaCl_2$ as a reactive salt. However, further experimental validations are desired. Specifically, the variation ranges of COP_t and η_{ex} are 0.49–0.53 and 0.79–0.84 for $SrBr_2$, 0.46–0.49 and 0.73–0.79 for LiOH, and 0.17–0.2, and 0.26–0.39 for $CaCl_2$, respectively.

3.4 Performance analysis of two-stage MBP-assisted cycle

To further enlarge the temperature lift of the MBP-assisted STHT system during the discharging process, a two-stage MBP-assisted STHT cycle with an intermediate cooler is proposed and evaluated using $SrBr_2$·(1-6)H_2O as reactive salt. The schematic diagram of the two-stage compression STHT cycle with an intermediate cooler and its corresponding P-T diagram is illustrated in Figure 9. The vapor at P_m from the evaporator is first pressurized to an intermediate pressure of P_{h1} by the first-stage compression process using MBP1, as shown in Figure 9A. The superheated vapor at T_{sv1} flows into the intercooler where a HTF circulates at ambient temperature. Subsequently, it is cooled to an unsaturated vapor at a lower temperature level of T_{sv2} while maintaing constant pressure. Next, the vapor at P_{h1} and T_{sv2} is directed into the second-stage compression process. Here, it undergoes compression to a higher pressure of P_{h2} by MBP2 before being introduced into the reactor. Due to the increase in pressure difference, there is an increase in heat output temperature ΔT_2 as compared to the single-stage compression process, as indicated in Figure 9B.

In this work, the temperature drop generated by the intercooler, i.e., T_{sv1}-T_{sv2}, is assumed to be 0.8 (T_{sv1}-T_{sat1}). Hence, the following equation can calculate the suction temperature T_{sv2} of MBP2:

$$T_{sv2} = 0.2T_{sv1} + 0.8T_{sat1} \quad (15)$$

where T_{sat1} is the saturation temperature corresponding to P_{h1}.

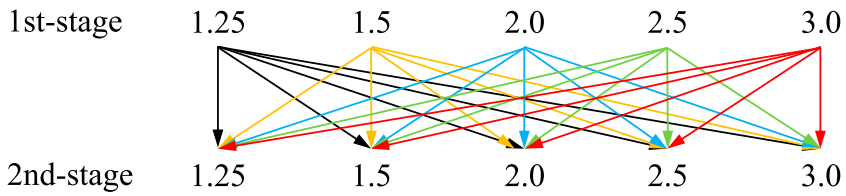

FIGURE 10
Compression ratio setting of each stage in the two-stage MBP-assisted STHT.

The corresponding conditions of the two-stage compression cycle are set as follows: evaporating temperature of 30°C, reaction advancement of 0.8, MBP isentropic efficiency of 70%, and the Cr range of 1.25–3.0. The detailed Cr setting of each stage is depicted in Figure 10 for ease of interpretation. The saturated vapor from the evaporator is first pressurized by a Cr range from 1.25 to 3.0, the same setting as the single-stage compression cycle. After intercooling, the unsaturated vapor is further compressed to a higher-pressure level with the Cr varies in the identical range as the first stage (e.g., compresses the vapor at Cr of 1.25 at the first stage, and then further compresses it by changing Cr from 1.25 to 3.0 at the second stage, and so on). The overall Cr of the two-stage MBP-assisted STHT cycle, the product of the individual compression ratios, is determined as follows.

$$C_{ro} = C_{r1} \cdot C_{r2} = \frac{P_{h2}}{P_m} \tag{16}$$

Figure 11A graphically demonstrates the variations of the heat output temperature (left-hand ordinate, blue lines) and the MBP discharge temperature at the second-stage compression process (right-hand ordinate, red lines) with Cr. It indicates that the heat output temperature range can be expanded from 62°C to 78°C in the single-stage compression cycle to 68°C–95°C in the two-stage compression cycle. However, the MBP discharge temperature increases more in the second-stage cycle than in the first stage due to the higher suction temperature of T_{sv2} as presented in Figure 11A, reaching a maximum value of 228°C when both the first and second-stage compression ratios are 3.0 far exceeds the allowed MBP operating temperature threshold.

Furthermore, it should be noted that $SrBr_2{\cdot}6H_2O$ has a melting point of 89°C (Stengler et al., 2020). Therefore, to ensure the safe and efficient operation of MBP-assisted STHT when using $SrBr_2{\cdot}H_2O$ as reactive salt, it is necessary to simultaneously consider the maximum allowable MBP discharge temperature and the melting temperature of $SrBr_2{\cdot}6H_2O$. The maximum feasible compression ratios and their corresponding heat output temperatures are determined by taking into account the limitations imposed by the melting temperature and the MBP discharge temperature, as depicted in Figure 11B. It can be observed that the maximum operable Cr of the second stage gradually decreases as the first-stage Cr increases. More specifically, the maximum second-stage compression ratios with their heat output temperatures are 3.0 (81°C), 2.86 (83°C), 2.57 (86°C), 2.36 (88°C), 2.0 (88.7°C) for the first-stage compression ratios of 1.25, 1.5, 2.0, 2,5, and 3.0, respectively. In addition, it can be found that cycles with the same overall Cr have the same heat output temperature due to the same discharge pressure. For example, a two-stage compression cycle with a Cr of 1.25 at the first stage and a Cr of 3.0 at the second stage would result in the same heat output temperature of 81°C as a two-stage cycle with a first-stage Cr of 3.0 and a second-stage Cr of 1.25.

Figure 12 depicts the changes in system efficiencies with respect to the second-stage Cr. In comparison to the single-stage compression cycle, the two-stage compression cycle, as shown in Figures 12A, C, experiences lower COP_e and η_{ex} due to an increased requirement for electrical power. The incremental reductions in the COP_e are noticeable with rising Cr, ranging from 20.5% to 84.4%. Nonetheless, a minimum COP_e of 8.31 could be obtained within the operable Cr range, comparable to that of the vapor compression heat pump. In contrast, the decreases in η_{ex} are relatively small, ranging from 3.46% to 9.0% with a minimum value of 0.65.

Similar to the single-stage MBP-assisted cycle, the COP_t of the two-stage compression cycle increases with the Cr, as revealed in Figure 12B. Compared to the single-stage compression cycle, the COP_t first decreases and then increases with increasing Cr. For instance, the COP_t decreases slightly from 0.503 (single-stage cycle at Cr of 1.25) to 0.499 (two-stage cycle at the second-stage Cr of 1.25 when the first-stage Cr is 1.25) and then increases to a maximum value of 0.513 at Cr of 3.0. This is because the negative effect resulting from the increase in electricity consumption is more significant than the positive effect caused by the rising temperature of MBP discharge vapor at lower compression ratios. However, the scenario shifts as Cr increases because the higher MBP discharge temperature amplifies the impact of the positive effect compared to the influence resulting from increased electricity consumption, which remains consistent with that of the single-stage cycle. Overall, the COP_t will reduce by −2.0–6.6% compared to the single-stage cycle, where the negative number indicates an increase. The minimum COP_t value of 0.483 appears at the second-stage Cr of 1.25 when the first-stage CR is 3.0.

As mentioned earlier, the same overall Cr results in identical heat output temperatures. However, this does not apply to the system efficiencies, as evident from Figure 12. Again, utilizing the overall Cr of 3.75 as an example, the correlation outcomes for four different combinations of the first and second-stage compression ratios are consolidated in Table 2 to facilitate comparison. It indicates that a lower first-stage Cr and higher second-stage Cr leads to better system efficiencies. Unlike the second-stage compression cycle, the MBP discharge heat produced during the first-stage cycle is released through the intercooler, resulting in no contribution to the system's preheating. Consequently, for a given evaporating temperature and a heat output temperature (i.e., the

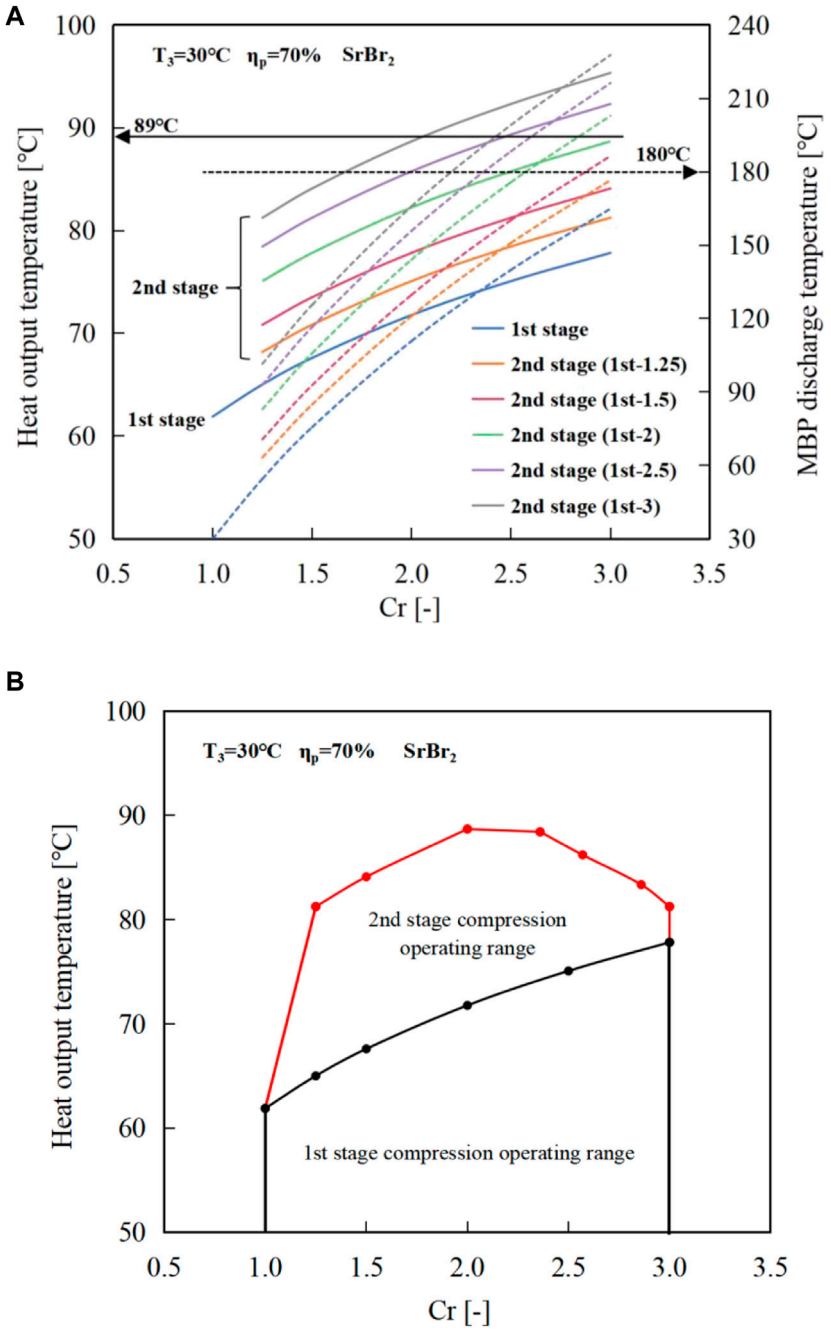

FIGURE 11
Variations of the **(A)** heat output temperature and MBP2 discharge temperature (Solid lines represent the heat output temperature; dashed lines indicate the MBP discharging temperature), **(B)** available operating range of the two-stage MBP-assisted STHT cycle using $SrBr_2$·(1-6)H_2O as reactive salt.

same overall Cr), the higher second-stage Cr would be preferred, demonstrating that the efficient utilization of MBP discharge heat has a potent role in improving the system performance.

In summary, increasing the number of compression stages contributes to the pressure level increment and thus can achieve a more significant heat output temperature. However, the operating domain of the proposed system becomes more restricted due to the limitation of the MBP discharge temperature and, in some cases, the thermodynamic property of the reactive material. Furthermore, this might necessitate a more intricate control strategy and a larger system size, which may not be suitable for building applications.

3.5 Economic and environmental analysis

The economics and environmental impact are acknowledged as two crucial aspects of developing energy systems. Electric water heater (EWH) and natural gas water heater (NGWH) are the two

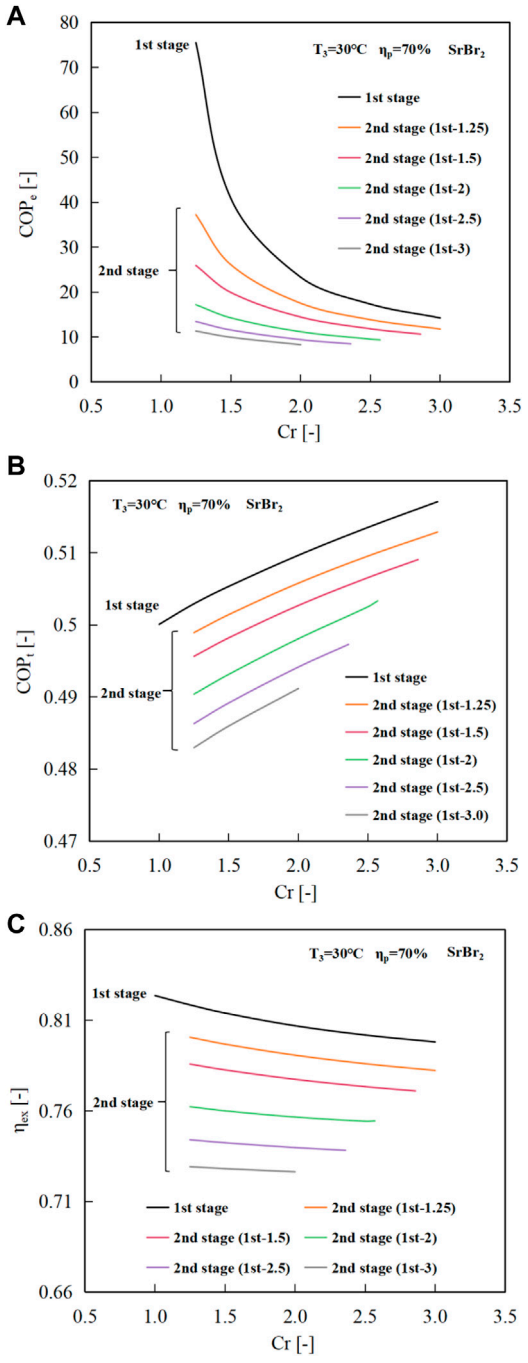

FIGURE 12
Variations of **(A)** COP_e, **(B)** COP_t, and **(C)** η_{ex} with the second-stage compression ratio at the evaporating temperature of 30°C.

most popular options for residential water heating. To provide more insight into the feasibility of the proposed system, the economic and environmental evaluation and comparison of the proposed system and the residential water heaters are conducted for household applications. Due to THT systems are still in the formative stage, system prices remain unknown. Therefore, some simplifications and assumptions are made to estimate the investment costs of energy systems.

TABLE 2 Comparison of system performances at different Cr combinations.

Cr	COP_e	COP_t	η_{ex}	T_d [°C]	W_p [kJ]
1st 1.25, 2nd 3.0	11.80	0.51	0.78	177	165.42
1st 1.5, 2nd 2.5	11.85	0.50	0.77	160	163.28
1st 2.5, 2nd 1.5	11.58	0.49	0.74	117	163.21
1st 3.0, 2nd 1.25	11.34	0.48	0.73	102	165.35

(1) The daily water heating energy for the systems assumes an upgrade from a 30°C input water temperature to a 70°C output temperature and the total hot water production of 50 gallons per day, which is the average usage for a household of 3–4 people.
(2) The mass ratio between the reactive material and reactor component is 1:1, and the reactor is assumed to be made of sus316, as described above in Section 2.2.
(3) The overall cost of the proposed system mainly includes the cost for the reactive materials, the MBP, the reactor, the evaporator/condenser, the water pump, the installation, and the balance of system (BOS).
(4) The BOS cost refers to the various supporting components costs, such as piping, valves, thermal insulating materials, controllers, etc., considering 20% of the capital cost (Cheng and Yin, 2023).
(5) The installation costs are assumed to 700 $ and 500 $ for EWH and NGWH, respectively (Carthan et al., 2023). However, an installation cost of 1200 $ is considered for the proposed system, which is higher than the reference ones due to the higher system complexity and technological immaturity.
(6) The annual maintenance cost is assumed to be 1.75% of the capital cost (Cheng and Yin, 2023).
(7) The energy efficiencies are set to 0.8, 0.95, and 0.9 for the proposed system, EWH, and NGWH, respectively.
(8) MBP's isentropic efficiency and Cr are assumed to be 70% and 2.5, respectively.

The parameters for the economic and environmental analysis are described in Table 3.

Given the above, the costs of the proposed system with three different reactive materials and the two reference systems were calculated, with the summarized results in Table 4. The proposed system using LiOH as the reactive material exhibits the highest investment cost, mainly due to the higher material cost of LiOH. Compared to $SrBr_2$ and LiOH, although $CaCl_2$ has the lowest material cost, a large amount of $CaCl_2$ results in a larger reactor volume and, thus, a higher reactor cost. According to the calculation results, the proposed systems have 1.78–2.03 times higher initial investment costs than the two reference systems. The higher initial investment cost is the primary concern hindering the market application of the proposed system, and therefore, the analysis of the system's payback period is required. The payback period is ratio of initial investment to annual saving, determining by the following equation.

$$PP = \frac{IC_{ps} - IC_{ref}}{C_{e,s} - (C_{m,ps} - C_{m,ref})}$$

where IC_{ps} and IC_{ref} are the investment costs of the proposed system and reference system, respectively; $C_{m,ps}$ and $C_{m,ref}$ are the annual

TABLE 3 Cost assumptions in the economic and environmental analysis.

Items	Value	Unit
$SrBr_2$	7 (Chemical Book, 2020)	$/kg
LiOH	30 (Alibaba, 2023)	$/kg
$CaCl_2$	0.15 (Made-in-China, 2023a)	$/kg
Stainless steel 316	1.5 (Made-in-China, 2023b)	$/kg
Evaporator/condenser	55 (Ostrava, 2023)	$
Water pump	120 (Amazon, 2023)	$
MBP	1000 (Made-in-China, 2023c)	$
EWH	779 (Lowe's, 2023a)	$
NGWH	919 (Lowe's, 2023b)	$
Installation cost of proposed system	1000	$
Installation cost of EWH	700	$
Installation cost of NGWH	500	$
BOS costs	20% of capital cost	$
Annual maintenance costs	1.75% of capital cost	$/year
Electricity price	0.142 (ElectricRate, 2023)	$/kWh
Natural gas price	0.118 (Global Petrol Prices, 2023)	$/kWh
CO_2 emissions factor - Anthracite	0.335 (OWID, 2017)	kg_{CO2}/kWh
CO_2 emissions factor - Natural gas	0.202 (OWID, 2017)	kg_{CO2}/kWh
Energy efficiency of proposed system	0.8	-
Energy efficiency of EWH	0.95	-
Energy efficiency of NGWH	0.9	-
Efficiency of electricity production	0.4	-
Number of operations	365	times/year

TABLE 4 Comparison of MBP-assisted STHT and residential water heaters in terms of economic and environmental performances.

Items	Unit	Single-stage MBP-assisted STHT			References system	
		$SrBr_2$	LiOH	$CaCl_2$	EWH	NGWH
Material cost	$	213.4	480.0	23.7	-	-
Stainless steel cost	$	45.7	24.0	236.6	-	-
Total investment cost	$	3292.7	3598.8	3294.1	1848.8	1773.8
Annual maintenance cost	$/year	57.6	63.0	57.6	32.4	31.0
Energy cost	$/year	33.7	35.9	68.0	479.3	420.5
Payback period (compared with EWH)	year	3.44	4.24	3.74	-	-
Payback period (compared with NGWH)	year	4.22	5.18	4.67	-	-
CO_2 reduction (compared with EWH)	ton/year	2.63	2.62	2.43	-	-
CO_2 reduction (compared with NGWH)	ton/year	0.64	0.63	0.56	-	-

maintenance costs for the proposed system and reference system, respectively; $C_{e,s}$ is annual energy saving for the proposed system compared to the reference system.

As can be seen from Table 4, the payback periods for the proposed systems are 3.44–4.24 years when compared with EWH and 4.22–5.18 years when compared with NGWH under the conditions

studied. Considering that the lifespan of a water heater is around 8–12 years, the proposed system is economically feasible.

It is worth mentioning that the system's technology readiness level should be considered during the economic analysis. Products with a higher degree of maturation, such as the two reference systems, are unlikely to reduce prices substantially. In contrast, however, TCESs are still in the research and development stage, offering the possibility of notable price reduction with improved technologies, extended operation duration, increased system scale, customized components, and optimized system design. In addition, providing more funding for research and demonstration projects, exploring the incentive and investment support mechanisms, boosting consumers' environmental awareness, and implementing technology push and market pull policies will also help to facilitate the development of TCES technologies and reduce the upfront investment costs.

From the perspective of environmental concern, the CO_2 emissions reduction potential of an energy system is a vital parameter to consider. The CO_2 emission factors of 0.335 kg_{CO2}/kWh and 0.202 kg_{CO2}/kWh for anthracite (thermal power generation with efficiency of 0.4) and natural gas, respectively, are used to assess the CO_2 mitigation by the proposed system. It can be seen from Table 4 that about 2.43–2.63 ton/year CO_2 emissions reduction can be obtained by replacing EWH with the proposed systems. In contrast, the CO_2 emissions reduction potential is comparably low when replacing NGWH with the proposed systems (0.56–0.64 ton/year). During a system lifespan of 10 years, about 24.3–26.3 tons (EWH) and 5.6–6.4 tons (NGWH) of CO_2 emissions can be reduced. Generally, MBP-assisted STHT with $SrBr_2$ as the reactive material exhibits better economic and environmental performance than the other two materials under the conditions studied.

4 Conclusion

To promote the efficient utilization of low-grade solar thermal energy in buildings, a hybrid water-based STHT with an MBP between the evaporator and the reactor has been proposed and evaluated theoretically using three different reactive salts. The main conclusions are presented as follows.

1) The proposed single-stage MBP-assisted cycles exhibit good heat upgrading ability and flexibility during the discharging process in response to the user demand by controlling the Cr. Relative to the conventional cycle, the heat output temperatures for $SrBr_2$, LiOH, and $CaCl_2$ can be raised by up to 15–17°C, 17–19°C, and 23–26°C, respectively, within the investigated conditions.
2) Higher evaporating temperatures lead to more pronounced sensible heat losses and increased electricity consumption. Consequently, this diminishes the system efficiencies, even though higher heat output temperatures are achieved.
3) Compared to the conventional cycle, COP_t increases slightly with increasing Cr for the cycle using $SrBr_2$ or LiOH, thanks to the positive effect of the high discharge temperature of MBP. On the other hand, the cycle employing $CaCl_2$ experiences a slight decrease in COP_t due to the higher consumption of sensible heat. Under the given conditions, the COP_t varies from 0.49 to 0.53, 0.46–0.49, and 0.17–0.25for $SrBr_2$, LiOH, and $CaCl_2$, respectively.
4) Both the COP_e and η_{ex} decrease as Cr increases for all three reactive salts. The obtained COP_es are higher or comparable to those of conventional vapor compression heat pumps within the studied conditions, with a varied range of 78.8–13.7, 73.0–12.6, and 40.1–5.2 for $SrBr_2$, LiOH, and $CaCl_2$, respectively. For $SrBr_2$ and LiOH, higher η_{ex} can be acquired, ranging from 0.79 to 0.84 and 0.73–0.79, respectively, compared to that of 0.26–0.39 for $CaCl_2$.
5) A higher number of compression stages can achieve a more significant heat output temperature. A lower first-stage Cr is more favorable for a given overall compression ratio and evaporating temperature condition. Compared to the single-stage MBP-assisted cycle using $SrBr_2$, the heat output temperature can be increased by up to 3–16°C in a two-stage MBP-assisted cycle. However, the operating domain of the two-stage MBP-assisted cycle becomes more restricted due to the limitation of the MBP discharge temperature and the melting temperature of $SrBr_2.6H_2O$. The higher electricity consumption leads to the performance degradation up to a maximum of 6.6%, 84.4%, and 9.0% of the single-stage cycle for COP_t, COP_e, and η_{ex}, respectively.
6) Compared with EWH and NGWH systems, the MBP-assisted cycles are economically feasible and more environmentally friendly for residential water heating, with a payback period of less than 5.2 years and a CO_2 emissions reduction potential higher than 5.6 tons over an assumed lifespan of 10 years.

The MBP-assisted water-based STHT is a promising alternative for low-grade solar thermal energy storage and upgrade. It is one of the most effective ways of pushing forward the development and application of THT in buildings.

Data availability statement

The raw data supporting the conclusion of this article will be made available by the authors, without undue reservation.

Author contributions

Conceptualization, analysis and interpretation of data, TZ and NK; mathematical model, TZ and XY; visualization, XY and HH; writing—original draft, TZ and JL; writing—revise and editing, TZ, JW, and LD; funding acquisition, TZ, XY, and HH. All authors contributed to the article and approved the submitted version.

Funding

This research was supported by the Open Fund of Science and Technology on Thermal Energy and Power Laboratory (No. TPL 2020A02), the National Natural Science Foundation of China (Nos 52176091 and 52006158).

Conflict of interest

The authors declare that the research was conducted in the absence of any commercial or financial relationships that could be construed as a potential conflict of interest.

Publisher's note

References

Alibaba (2023). 56.5% lithium hydroxide. Available at: https://www.alibaba.com/product-detail/56-5-Lithium-hydroxide-with-Industrial_1600252229148.html?spm=a2700.galleryofferlist.normal_offer.d_title.78f318bd0A27Ex (Accessed August 25, 2023).

Amazon (2023). WASSERMANN RV water pump. Available at: https://www.amazon.com/WASSERMANN-Booster-Priming-Diaphragm-Pressure/dp/B0BFB1FMKV/ref=sr_1_4?crid=2FWW52EOU279N&keywords=water%2Bpump%2B11%2BGPM&qid=1693395508&sprefix=water%2Bpump%2B11%2Bgpm%2Caps%2C366&sr=8-4&th=1 (Accessed August 27, 2023).

An, G., Wang, L., and Zhang, Y. (2020). Overall evaluation of single-and multi-halide composites for multi-mode thermal-energy storage. *Energy* 212, 118756. doi:10.1016/j.energy.2020.118756

An, G., Wu, S., Wang, L., Zhang, C., and Zhang, B. (2022). Comparative investigations of sorption/resorption/cascading cycles for long-term thermal energy storage. *Appl. Energy* 306, 117991. doi:10.1016/j.apenergy.2021.117991

Babu, K. S., and Kumar, E. A. (2022). Thermodynamic analysis of compressor operated resorption thermochemical energy storage system for heat storage, combined cooling and heat upgradation. *J. Energy Storage* 50, 104659. doi:10.1016/j.est.2022.104659

Bamigbetan, O., Eikevik, T. M., Nekså, P., and Bantle, M. (2017). Review of vapour compression heat pumps for high temperature heating using natural working fluids. *Int. J. Refrig.* 80, 197–211. doi:10.1016/j.ijrefrig.2017.04.021

Carthan, A. (2023). Compare water heater installation cost. Available at: https://www.thisoldhouse.com/plumbing/reviews/water-heater-installation-cost (Accessed August 25, 2023).

Cheng, X., and Yin, Y. (2023). Performance analysis and optimization of a coupled open and close liquid desiccant sorption system using LiCl solution. *Appl. Therm. Eng.* 233, 121153. doi:10.1016/j.applthermaleng.2023.121153

Chemical Book (2020). Strontium bromide. Available at: https://www.chemicalbook.com/ProductDetail_EN_820572.htm (Accessed August 25, 2023).

Climate Watch (2023). Net-zero tracker. Available at: https://www.climatewatchdata.org/net-zero-tracker (Accessed June 3, 2023).

Daneshazarian, R., and Berardi, U. (2023). Nano-enhanced thermal energy storage coupled to a hybrid renewable system for a high-rise zero emission building. *Energy Convers. Manag.* 291, 117301. doi:10.1016/j.enconman.2023.117301

Di Fraia, S., Figaj, R. D., Filipowiczh, M., and Vanoli, L. (2022). "Chapter 6 - solar-based systems," in *Polygeneration systems: design, processes and technologies*. Editors F. Calise, M. Dentice D'Accadia, L. Vanoli, and M. Vicidomini (Cambridge: Academic Press), 193–237. doi:10.1016/B978-0-12-820625-6.00005-0

Ding, B., Xu, C., Liao, Z., and Ye, F. (2021). Study on long-term thermochemical thermal storage performance based on $SrBr_2$-expanded vermiculite composite materials. *J. Energy Storage* 42, 103081. doi:10.1016/j.est.2021.103081

Esaki, T., Yasuda, M., and Kobayashi, N. (2017). Experimental evaluation of the heat output/input and coefficient of performance characteristics of a chemical heat pump in the heat upgrading cycle of $CaCl_2$ hydration. *Energy Convers. Manag.* 150, 365–374. doi:10.1016/j.enconman.2017.08.013

Feng, W., Zhou, N., Wang, W., Khanna, N., Liu, X., and Hou, J. (2021). Pathways for accelerating maximum electrification of direct fuel use in China's building sector. Energy technologies area. *Berkeley Lab*. Available at: https://eta.lbl.gov/publications/pathways-accelerating-maximum.

Gao, J., Xu, Z., and Wang, R. (2021). Enlarged temperature lift of hybrid compression-absorption heat transformer via deep thermal coupling. *Energy Convers. Manag.* 234, 113954. doi:10.1016/j.enconman.2021.113954

Gao, P., Shao, L., and Zhang, C. (2019). Pressure boost thermochemical sorption heat pump cycle. *Energy* 169, 1090–1100. doi:10.1016/j.energy.2018.12.119

Global Petrol Prices (2023). Natural gas prices. Available at: https://www.globalpetrolprices.com/natural_gas_prices/(Accessed August 28, 2023).

Hong, H., Li, W., and Gu, C. (2018). Performance study on a mechanical vapor compression evaporation system driven by Roots compressor. *Int. J. Heat Mass Transf.* 125, 343–349. doi:10.1016/j.ijheatmasstransfer.2018.03.098

Hong, L., Zhou, N., Fridley, D., Feng, W., and Khanna, N. (2014). "Modeling China's building floor-area growth and the implications for building materials and energy demand," in Proceedings of the 2014 ACEEE Summer Study on Energy Efficiency in Buildings, 146–157. Available at:. http://aceee.org/files/proceedings/2014/data/papers/10-230.pdf. (Accessed. September. 1, 2023).

IEA (2021). An energy sector roadmap to carbon neutrality in China. Available at: https://www.iea.org/reports/an-energy-sector-roadmap-to-carbon-neutrality-in-china (Accessed April 10, 2023).

IEA (2022). Heating. Available at: https://www.iea.org/fuels-and-technologies/heating (Accessed April 10, 2023).

Jiang, L., Li, S., Wang, R., Fan, Y., Zhang, X., and Roskilly, A. P. (2021). Performance analysis on a hybrid compression-assisted sorption thermal battery for seasonal heat storage in severe cold region. *Renew. Energy* 180, 398–409. doi:10.1016/j.renene.2021.08.101

Jiang, L., Wang, L., Wang, R., Zhu, F., Lu, Y., and Roskilly, A. P. (2017). Experimental investigation on an innovative resorption system for energy storage and upgrade. *Energy Convers. Manag.* 138, 651–658. doi:10.1016/j.enconman.2017.02.014

Jiang, L., Wang, R., Tao, X., and Roskilly, A. P. (2020). A hybrid resorption-compression heat transformer for energy storage and upgrade with a large temperature lift. *Appl. Energy* 280, 115910. doi:10.1016/j.apenergy.2020.115910

Li, T., Wang, R., and Kiplagat, J. K. (2013). A target-oriented solid-gas thermochemical sorption heat transformer for integrated energy storage and energy upgrade. *AIChE J.* 59 (4), 1334–1347. doi:10.1002/aic.13899

Li, T., Wang, R., and Yan, T. (2015). Solid-gas thermochemical sorption thermal battery for solar cooling and heating energy storage and heat transformer. *Energy* 84, 745–758. doi:10.1016/j.energy.2015.03.040

Li, T., Wu, S., Yan, T., Xu, J., and Wang, R. (2016). A novel solid-gas thermochemical multilevel sorption thermal battery for cascaded solar thermal energy storage. *Appl. energy* 161, 1–10. doi:10.1016/j.apenergy.2015.09.084

Li, W., Klemeš, J. J., Wang, Q., and Zeng, M. (2021). Characterisation and sorption behaviour of LiOH-LiCl@ EG composite sorbents for thermochemical energy storage with controllable thermal upgradeability. *Chem. Eng. J.* 421, 129586. doi:10.1016/j.cej.2021.129586

Lowe's (2023b). A.O. Smith signature 100 50-gallon tall 9-year limited 40000-BTU natural gas water heater. Available at: https://www.lowes.com/pd/A-O-Smith-Signature-Select-50-Gallon-Tall-9-Year-Limited-Natural-Gas-Water-Heater/1000550955 (Accessed August 28, 2023).

Lowe's (2023a). A.O. Smith signature 300 50-gallon tall 9-year limited warranty 5500-watt double element smart electric water heater. Available at: https://www.lowes.com/pd/A-O-Smith-A-O-Smith-Signature-300-Series-50-Gallon-Tall-iCOMM-8482-Smart-Connectivity-9-Year-5500-Watt-Double-Element-Electric-Water-Heater/5005423741 (Accessed August 28, 2023).

Made-in-China (2023a). Calcium chloride anhydrous. Available at: https://saltsuppliers.en.made-in-china.com/product/OChmAdMbLocE/China-Food-Grade-Industrial-Grade-Factory-Price-Calcium-Chloride-Anhydrous-94-.html (Accessed August 25, 2023).

Made-in-China. (2023c). Roots vacuum pump. Available at: https://pransch.en.made-in-china.com/product/bwPTMqXuEHWr/China-Light-Industry-Bypass-Valve-Vacuum-Furnace-Freez-Infusion-Degassing-Distillation-Laminating-Removal-Package-Coating-Dry-Mechanical-Boosters-Blower-Roots-Pump.html (Accessed August 27, 2023).

Made-in-China (2023b). SS316L plates sheets price. Plate Pipe. Available at: https://hongshuoweiye.en.made-in-china.com/product/dwGaZKPYfDrM/China-Big-Discount-Ss201-SS304-SS316-SS304L-SS316L-Ss430-Ss410-Ss420-Ss409-Ss310s-Ss904L-Plates-Sheets-Price-Thickness-18gauge-to-20gauge-Sheet-Plate-Pipe.html (Accessed August 24, 2023).

Michel, B., and Clausse, M. (2020). Design of thermochemical heat transformer for waste heat recovery: methodology for reactive pairs screening and dynamic aspect consideration. *Energy* 211, 118042. doi:10.1016/j.energy.2020.118042

Mohan, M., and Sharma, V. K. (2019). Studies on thermodynamic performance of three stage sorption heat transformer. *Appl. Therm. Eng.* 154, 228–237. doi:10.1016/j.applthermaleng.2019.03.080

N'Tsoukpoe, K. E., Mazet, N., and Neveu, P. (2016). The concept of cascade thermochemical storage based on multimaterial system for household applications. *Energy Build.* 129, 138–149. doi:10.1016/j.enbuild.2016.07.047

Nguyen, M. H., Zbair, M., Dutournié, P., Gervasini, A., Vaulot, C., and Bennici, S. (2022). Toward new low-temperature thermochemical heat storage materials: investigation of hydration/dehydration behaviors of MgSO4/Hydroxyapatite composite. *Sol. Energy Mater. Sol. Cells* 240, 111696. doi:10.1016/j.solmat.2022.111696

Ostrava, V. Z. H. (2023). SWEP E6THx14 Heat exchanger. Available at: https://www.heat-exchangers.uk/shop/exchanger.php?vymenik=E6TH&desek=14 (Accessed August 24, 2023).

Our world in data (2017). Carbon dioxide emissions factor. Available at: https://ourworldindata.org/grapher/carbon-dioxide-emissions-factor (Accessed August 28, 2023).

Richter, M., Habermann, E. M., Siebecke, E., and Linder, M. (2018). A systematic screening of salt hydrates as materials for a thermochemical heat transformer. *Thermochim. Acta* 659, 136–150. doi:10.1016/j.tca.2017.06.011

Shahzad, M. W., Burhan, M., Ang, L., and Ng, K. C. (2017). Energy-water-environment nexus underpinning future desalination sustainability. *Desalination* 413, 52–64. doi:10.1016/j.desal.2017.03.009

Sharma, R., and Anil Kumar, E. (2017). Study of ammoniated salts based thermochemical energy storage system with heat up-gradation: a thermodynamic approach. *Energy* 141, 1705–1716. doi:10.1016/j.energy.2017.11.015

Stengler, J., Bürger, I., and Linder, M. (2021). Performance analysis of a gas-solid thermochemical energy storage using numerical and experimental methods. *Int. J. Heat Mass Transf.* 167, 120797. doi:10.1016/j.ijheatmasstransfer.2020.120797

Stengler, J., Bürger, I., and Linder, M. (2020). Thermodynamic and kinetic investigations of the $SrBr_2$ hydration and dehydration reactions for thermochemical energy storage and heat transformation. *Appl. Energy* 277, 115432. doi:10.1016/j.apenergy.2020.115432

Su, C., and Urban, F. (2021). Carbon neutral China by 2060: the role of clean heating systems. *Energies* 14 (22), 7461. doi:10.3390/en14227461

Vérez, D., Borri, E., Zsembinszki, G., and Cabeza, L. F. (2023). Thermal energy storage co-benefits in building applications transferred from a renewable energy perspective. *J. Energy Storage* 58, 106344. doi:10.1016/j.est.2022.106344

Wang, X., Yu, B., An, R., Sun, F., and Xu, S. (2022). An integrated analysis of China's iron and steel industry towards carbon neutrality. *Appl. Energy* 322, 119453. doi:10.1016/j.apenergy.2022.119453

Wei, S., Han, R., Su, Y., Zhou, W., Li, J., Su, C., et al. (2020). Development of pomegranate-type $CaCl_2$@C composites via a scalable one-pot pyrolysis strategy for solar-driven thermochemical heat storage. *Energy Convers. Manag.* 212, 112694. doi:10.1016/j.enconman.2020.112694

Wu, W., You, T., Wang, J., Wang, B., Shi, W., and Li, X. (2018). A novel internally hybrid absorption-compression heat pump for performance improvement. *Energy Convers. Manag.* 168, 237–251. doi:10.1016/j.enconman.2018.05.007

Wyttenbach, J., Bougard, J., Descy, G., Skrylnyk, O., Courbon, E., Frère, M., et al. (2018). Performances and modelling of a circular moving bed thermochemical reactor for seasonal storage. *Appl. Energy* 230, 803–815. doi:10.1016/j.apenergy.2018.09.008

Yan, T., Kuai, Z., and Wu, S. (2020). Multi-mode solid–gas thermochemical resorption heat transformer using $NiCl_2$-$SrCl_2$/NH_3. *Appl. Therm. Eng.* 167, 114800. doi:10.1016/j.applthermaleng.2019.114800

Zeng, T., Esaki, T., Li, J., Kobayashi, N., and Huang, H. (2017). Evaluation of performance of thermal and electrical hybrid adsorption chiller cycles with mechanical booster pumps. *J. Mater. Sci. Chem. Eng.* 5 (5), 22–32. doi:10.4236/msce.2017.55003

Zeng, T., Li, J., Deng, L., He, Z., Kobayashi, N., Wu, R., et al. (2022). Mechanical booster pump-assisted thermochemical mode for low-grade heat storage and upgrading: a thermodynamic study. *Front. Energy Res.* 10, 851611. doi:10.3389/fenrg.2022.851611

10.3389/fenrg.2023.1236436

Nomenclature

P	pressure, kPa
T	temperature, K
R	ideal gas molar constant, J/(mol·K)
ΔH_r	standard enthalpy of reaction, J/mol
ΔS_r	standard entropy of reaction, J/(mol·K)
Q	amount of energy, J
ΔN_{H2O}	theoretical molar amount of water vapor, mol
$c_{p,M\cdot xH2O}$	specific heat of anhydrous or less hydrous salt, kJ/(mol·K)
$c_{p,M\cdot(x+y)H2O}$	specific heat of hydrated salt, kJ/(mol·K)
$c_{p,r}$	specific heat of reactor metal, kJ/(mol·K)
v_{H2O}	stoichiometric coefficient
m_r	mass of the reactor metal, kg
$c_{p,l}$	specific heat of liquid water, kJ/(mol·K)
ΔH_{vap}	vaporization enthalpy of water, kJ/mol
$c_{p,v}$	specific heat of water vapor at MBP discharge, kJ/(kg·K)
Cr	compression ratio of MBP
COP_t	coefficient of performance baaed on the total energy input
COP_e	coefficient of performance based on the electricity input
Greek	symbols
η_r	reaction advancement
η_p	isentropic efficiency of MBP
η_{ex}	exergy efficiency
κ	adiabatic index
Abbreviations	
THT	thermochemical heat transformers
MBP	mechanical booster pump
GHG	global greenhouse gas
TCES	thermochemical energy storage
STHT	sorption thermochemical heat transformer
RTHT	resorption thermochemical heat transformer
HTF	heat transfer fluid
BOS	balance of system
EWH	electric water heater
NGWH	natural gas water heater